

# Optical and Modeling Studies of Sodium/Halide Reactions for the Formation of Titanium and Boron Nanoparticles

Kristen L. Steffens<sup>†</sup> and Michael R. Zachariah\*

*Chemical Science and Technology Laboratory, National Institute of Standards and Technology, Gaithersburg, Maryland 20899*

Douglas P. DuFaux and Richard L. Axelbaum

*Department of Mechanical Engineering, Washington University, St. Louis, Missouri 63130*

*Received February 1, 1996. Revised Manuscript Received May 16, 1996<sup>Ⓢ</sup>*

This study focuses on the optical characterization of a method for the formation of nanoscale titanium and boron particles. This versatile method can also be used to form a variety of metals as well as ceramic powders such as TiB<sub>2</sub>. The gas-phase chemical process, given by  $(mn)\text{Na} + (n)\text{MCl}_m \rightarrow (\text{M})_n + (mn)\text{NaCl}$ , should be generic to many metal chlorides or mixtures of metal chlorides. In this study, either TiCl<sub>4</sub> or BCl<sub>3</sub> is reacted with Na vapor in a counterflow diffusion flame reactor. After the Cl is stripped from the metal chloride by the Na vapor, nanosize Ti or B particles form and, under certain thermodynamic circumstances, become encased in NaCl, which helps to prevent agglomeration and postflame oxidation. The two-dimensional spatial distribution of Na<sub>2</sub> has been optically interrogated using planar laser-induced fluorescence under various conditions to clarify the influence of concentration and transport on particle formation. Reactant concentration and time available for reaction were found to dramatically influence the reactive flow. Simulations using a counterflow diffusion flame model show that formation of TiB<sub>2</sub> likely occurs by gas-phase clustering reactions involving both precursors. The model indicates that experimental results are consistent with the proposed chlorine abstraction mechanism with near-collisional reaction rates.

## Introduction

Nanoscale materials can have 50% of their atoms located in the grain boundaries.<sup>1</sup> Thus, these materials are expected to have size-dependent properties and potential benefits<sup>2</sup> over conventional micron-grained materials. Nanoscale materials have been observed to have increased ductility<sup>1–4</sup> and lower processing temperatures<sup>1,2,5</sup> for ceramics, increased low-temperature strength<sup>2</sup> and GMR (giant magneto resistance)<sup>6</sup> for metals, and higher strength at high temperatures for composite nanomaterials.<sup>7</sup> There are a number of methods of synthesizing the nanoparticles that are consolidated into the nanoscale materials, including gas-phase condensation,<sup>5,8</sup> solution-phase processing,<sup>9</sup> and combustion synthesis.<sup>10,11</sup>

A relatively new synthesis route<sup>12–14</sup> involves reacting alkali metals such as Na or K with metal halides to yield the metal and an alkali halide salt. Such reactions<sup>15,16</sup> have been known for many years; the earliest extensive study on the reactions of Na with metal chlorides was published in 1936 by Heller and Polanyi.<sup>17</sup> Since then, further studies on this type of chemistry have been performed,<sup>18</sup> but recently there has been interest in applying this chemistry to materials synthesis.<sup>12–14,19</sup> Calcote and Felder<sup>12</sup> were the first to demonstrate the potential of this approach by producing photovoltaic grade Si plate via the gas-phase reaction of SiCl<sub>4</sub> and Na. A slightly different approach was used by Glassman et al.,<sup>13</sup> who produced ceramic and intermetallic

(11) Zachariah, M. R.; Aquino, M. I.; Shull, R. D.; Steel, E. B. *Nanostruct. Mater.* **1995**, *5*, 383.

(12) Calcote, H. F.; Felder, W. Twenty-Fourth Symposium (International) on Combustion; The Combustion Institute: Pittsburgh, 1992; p 1869.

(13) Glassman, I.; Davis, K. A.; Brezinsky, K. Twenty-Fourth Symposium (International) on Combustion; The Combustion Institute: Pittsburgh, 1992; p 1877.

(14) DuFaux, D. P.; Axelbaum, R. L. *Combust. and Flame* **1995**, *100*, 350.

(15) Mellor, J. W. *A Comprehensive Treatise on Inorganic and Theoretical Chemistry*; Longmans, Green and Co.: New York, 1922; Vol. II.

(16) Polanyi, M.; Schay, G. *Z. Phys.* **1928**, *47*, 814.

(17) Heller, W.; Polanyi, M. *Faraday Society Trans.* **1936**, *32*, 633.

(18) Naegeli, D. W.; Palmer, H. B., Eleventh Symposium (International) on Combustion; The Combustion Institute, Pittsburgh 1967; p 1161.

(19) Olson, D. B.; Miller, W. J.; Gould, R. K. Silicon Halide-Alkali Metal Flames as a Source of Solar Grade Silicon; *TP-395*; AeroChem, 1980.

<sup>†</sup> NRC/NIST Postdoctoral Research Associate 1995–present.

\* To whom correspondence should be addressed.

<sup>Ⓢ</sup> Abstract published in *Advance ACS Abstracts*, July 15, 1996.

(1) Siegel, R. W. *Mater. Sci. Forum* **1989**, *37*, 299.

(2) Gleiter, H. In *Science of Advanced Materials: 1988 ASM Materials Science Seminar*; Weidersich, H., Meshii, M., Eds.; ASM International, Materials Park, OH, 1988.

(3) Karch, J.; Birringer, R.; Gleiter, H. *Nature* **1987**, *330*, 556.

(4) Gleiter, H. *Nanostruct. Mater.* **1992**, *1*, 1.

(5) Siegel, R. W. *Annu. Rev. Mater. Sci.* **1991**, *21*, 559.

(6) Dagani, R. *Chem. Eng. News* **1992**, *70*, 18.

(7) Sastry, S. M. L.; Peng, T. C.; Lederich, R. J. In *Mechanical Behavior of Rapidly Solidified Materials*; Sastry, S. M. L., MacDonald, B. A., Eds.; AIME: Warrendale, PA, 1986; p 207.

(8) Gleiter, H. *Prog. Mater. Sci.* **1990**, *33*, 223.

(9) Bates, S. E.; Buhro, W. E.; Frey, C. A.; Sastry, S. M. L.; Kelton, K. F. *J. Mater. Res.* **1995**, *10*, 2599.

(10) McMillin, B. K.; Biswas, P.; Zachariah, M. R. *J. Mater. Res.* **1996**, *11*, No. 6.

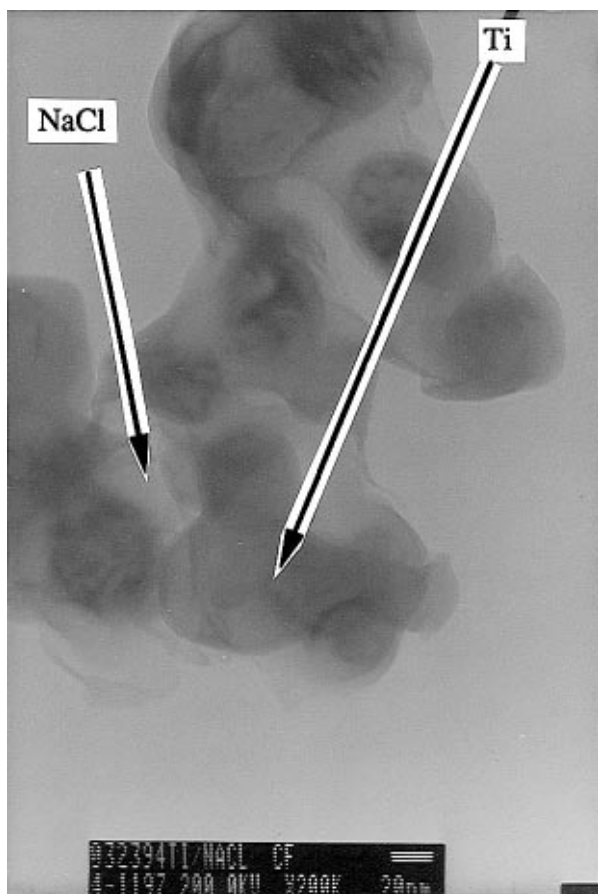
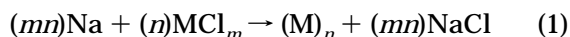


**Figure 1.** TEM image of particles made by DuFaux and Axelbaum in a coflow reactor showing unagglomerated nanoscale Ti particles (dark areas) encased in NaCl (light gray areas).

particles by combusting NaK droplets in atmospheres of metal halide vapors. Most recently, DuFaux and Axelbaum<sup>14,20</sup> have developed a number of gas-phase diffusion flames in which they react Na with metal halides to make unagglomerated non-oxide nanoscale materials.

In this study, heated Na was reacted with either heated  $\text{BCl}_3$  or  $\text{TiCl}_4$  to form nanoscale titanium or boron particles in a counterflow diffusion flame arrangement. The gas-phase chemical process is given by eq 1, where M represents Ti or B. The Na strips Cl



atoms from the metal chloride, leaving metal atoms which nucleate to form nanosize Ti or B particles. Under specific thermodynamic conditions detailed in DuFaux and Axelbaum,<sup>14</sup> nanosize particles can be encased in NaCl, which serves to prevent agglomeration and postflame oxidation of air-sensitive particles. Figure 1 shows a TEM image of unagglomerated nanoscale Ti particles encased in a protective coating of NaCl (as determined by EDS), collected in a coflow reactor.<sup>14</sup> This versatile method of materials synthesis has also been used to form  $\text{TiB}_2$  by reacting a mixture of  $\text{TiCl}_4$  and  $\text{BCl}_3$  with Na vapor.<sup>14</sup>

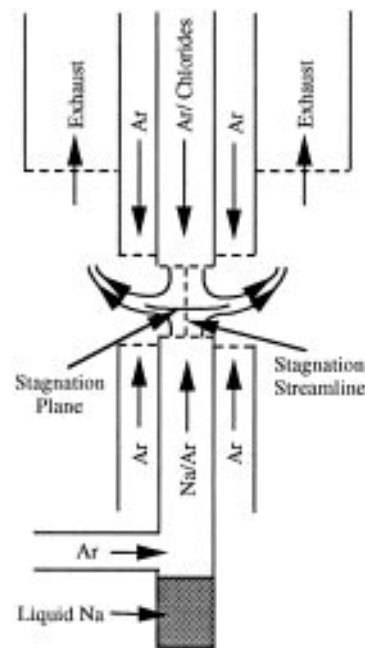


**Figure 2.** Schematic diagram of counterflow diffusion flame.

In this study, laser-based diagnostics are performed on the reacting flow to characterize the spatial distribution of the reactive species for various flow rates, reactant concentrations, and temperatures. Planar laser-induced fluorescence (PLIF) is a laser-based technique which has been shown to be useful in characterizing species concentrations in reactive flows.<sup>10,21</sup> We chose to measure Na dimer ( $\text{Na}_2$ ) concentration by PLIF to provide insight into the reaction of Na with  $\text{TiCl}_4$  and  $\text{BCl}_3$ .

Computer modeling is performed on the reacting system, using a counterflow diffusion code, to provide insight into the interaction of Na with  $\text{TiCl}_4$  and  $\text{BCl}_3$  in the counterflow diffusion flame. The modeling is employed to help determine rate-limiting processes and to provide insight into the likely mechanism of particle nucleation.

## Experimental Section

**Counterflow Reactor.** A counterflow diffusion flame reactor was used in these experiments, because it affords advantages over the more traditional coflow diffusion flame geometry. In particular, the counterflow diffusion flame is effectively a one-dimensional system along the stagnation streamline.<sup>22</sup> Thus, experiments and models are greatly simplified and can be accurately compared.<sup>23</sup>

Experiments were performed in the counterflow diffusion flame reactor pictured schematically in Figure 2. The counterflow diffusion flame system consists of two counterpropagating flows, each containing a different reactant. Chemical reaction occurs near the stagnation plane with the exact location of the reaction zone being dependent on diffusivities, flow rates, separation distance, chemical reaction rates, and reactant concentrations. Axial velocities necessarily go to zero at the stagnation plane, and particulates formed in the reaction zone are swept into the stagnation plane and away from the axial centerline. The reactor consists of an upper and a lower half, mounted in a stainless steel vacuum housing.

(21) McMillin, B. K.; Zachariah, M. R. *J. Appl. Phys.* **1995**, *77*, 1.

(20) Axelbaum, R. L.; DuFaux, D. P.; Frey, C. A.; Kelton, K. F.; Lawton, S. A.; Rosen, L. J.; Sastry, S. M. L. *J. Mater. Res.* **1996**, *11*, 948.

(22) Smooke, M. D.; Puri, I. K.; Seshadri, K., Twenty-First Symposium (International) on Combustion; The Combustion Institute, Pittsburgh 1986; p 1783.

(23) Zachariah, M. R.; Semerjian, H. G. *AIChE J.* **1989**, *35*, 2003.

Although the reactor has been designed to allow for operation under vacuum, the system was operated under atmospheric conditions for the present study. Each half of the reactor has a central flow tube of inner diameter 1.16 cm surrounded by a concentric annulus of inner diameter 2.67 cm. The distance between the upper and lower central tubes was set to 1.10 cm with the reactor at its working temperature. Dilute mixtures of  $\text{TiCl}_4$  and Ar were obtained by bubbling Ar through room-temperature  $\text{TiCl}_4$  and then further diluting with Ar.  $\text{BCl}_3$  was controlled directly with a rotameter and subsequently diluted with Ar. The metal chloride/Ar flow was then delivered through the central tube in the upper half of the reactor, surrounded by an annulus of Ar. For delivery of the gaseous Na/Ar mixture, heated Ar was passed over a heated reservoir of molten Na inside the lower half of the reactor where it became partially saturated with Na vapor. The Na/Ar flow was then delivered through the central tube in the lower half of the reactor, surrounded by an annular flow of Ar. The product gases and particles were exhausted through the upper half of the reactor using a mechanical pump. To ensure stable flows, honeycomb flow-straighteners were placed in all four flow tubes. Porous disks were needed in the Ar shroud flow tubes prior to the honeycomb to minimize flow irregularities. All flow rates were measured with calibrated rotameters or flow controllers. The Na reservoir and the central and outer flow tubes in both the top and bottom halves of the reactor were heated and were monitored using type K thermocouples. A fine-wire type R thermocouple was used to check the temperature of the gases as they exit the upper and lower central flow tubes and throughout the reaction zone. For all experiments presented here, the exit temperature for all flows was kept at  $780 \pm 10$  K, and the temperature profile across the reaction zone was flat.

**Na<sub>2</sub> Spectroscopy.** Na has an extremely high absorption cross section, which makes it difficult to measure quantitatively except in very dilute concentrations; however, Na concentration can be related to Na<sub>2</sub> concentration by a known<sup>24</sup> temperature-dependent equilibrium constant. At 780 K, Na<sub>2</sub> is present at 1% of the concentration of Na when the concentration of Na in Ar is 0.1%. At these concentrations, linear optical measurements of Na<sub>2</sub> are easily performed, so PLIF was used to make spatially resolved measurements.

The technique of laser-induced fluorescence (LIF) is illustrated using the schematic potential energy diagram of the ground  $X^1\Sigma^+$  and excited  $B^1\Pi_u$  electronic states of Na<sub>2</sub> in Figure 3. When a photon of the proper wavelength (488 nm in this case) encounters a gas-phase Na<sub>2</sub> molecule, the photon can be absorbed by the Na<sub>2</sub> molecule. Na<sub>2</sub> is excited from a specific vibrational and rotational level in the  $X^1\Sigma^+$  ground electronic state to a specific vibrational and rotational level in the  $B^1\Pi_u$  excited electronic state. Excited Na<sub>2</sub> can subsequently emit photons and drop back down to one of a variety of rotational and vibrational levels in the  $X^1\Sigma^+$  ground electronic state. These emitted photons have wavelengths between 465 and 545 nm and form the fluorescence signal, whose intensity is directly proportional to the number of Na<sub>2</sub> molecules initially in the ground electronic state. Thus, LIF is used to measure the relative concentration of the ground-state Na<sub>2</sub> species.

Preliminary LIF experiments were conducted to characterize the fluorescence signal. The emitted light was collected, dispersed in a 1.6 nm/mm resolution monochromator and detected with a photomultiplier tube (PMT). The spectrum in Figure 4 was obtained by exciting Na<sub>2</sub> at 488 nm and scanning the monochromator between wavelengths of 465 and 555 nm with a resolution of about 0.38 nm. The wavelength of the detected fluorescence was calibrated to the 488 nm scattered laser light peak, labeled in Figure 4. The fluorescence spectrum shown was not corrected for the wavelength-dependent response of the monochromator grating and was not normalized to slight drift in laser power, since it was only

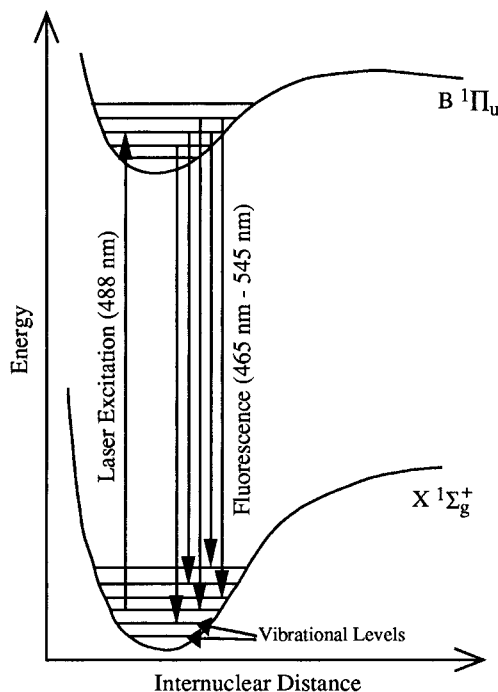


**Figure 3.** Schematic potential energy diagram for the ground  $X^1\Sigma^+$  and excited  $B^1\Pi_u$  electronic states of Na<sub>2</sub>, showing vibrational levels to illustrate the LIF method.

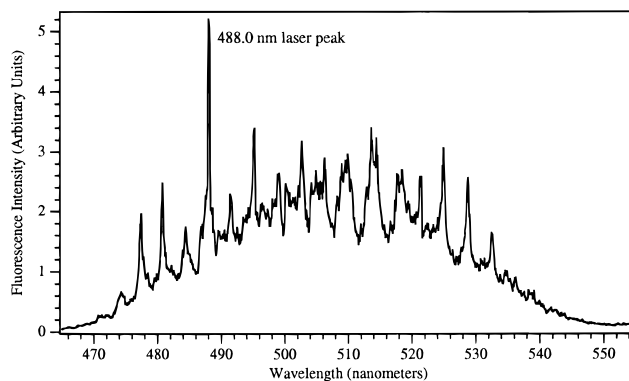


**Figure 4.** Na<sub>2</sub> fluorescence spectrum taken while exciting with 488 nm light and scanning monochromator with a resolution of about 0.38 nm.

used to identify the fluorescence as coming from Na<sub>2</sub>. As seen in Figure 4, fluorescence is observed between wavelengths of 465 and 545 nm. The signal was found to be linear with laser power and was present only when Na/Na<sub>2</sub> vapor was present.

The spectroscopy of the B–X transition of Na<sub>2</sub> has been studied by many groups.<sup>25–30</sup> The work by Kusch and Hessel<sup>25</sup> (KH), who used 488 nm argon ion laser light to excite Na<sub>2</sub> to determine its spectroscopic constants, is most appropriate to consider for comparison with this work. KH<sup>25</sup> observed Na<sub>2</sub> vapor at 850 K in 2000 Pa (15 Torr) of buffer gas and used a laser whose line width was smaller than the interval between rotational levels, as was the case for this work. They found<sup>25</sup> that individual rotational lines were excited out of the overlapping ground state vibrational levels ranging from  $v' = 0$  to  $v' = 17$  to populate excited state vibrational levels between  $v = 3$  and  $v = 27$ . Following excitation, vibrational and rotational

(25) Kusch, P.; Hessel, M. M. *J. Chem. Phys.* **1978**, *68*, 2591.

(26) Fredrickson, W. R.; Watson, W. W. *Phys. Rev.* **1927**, *30*, 429.

(27) Loomis, F. W.; Wood, R. W. *Phys. Rev.* **1928**, *32*, 223.

(28) Demtroder, W.; McClintock, M.; Zare, R. N. *J. Chem. Phys.* **1969**, *51*, 5495.

(29) Demtroder, W.; Stock, M. *J. Mol. Spectrosc.* **1975**, *55*, 476.

(30) Konowalow, D. D.; Rosenkrantz, M. E.; Olson, M. L. *J. Chem. Phys.* **1980**, *72*, 2612.

(24) Gordon, S.; McBride, B. J. Computer Program for Calculation of Complex Chemical Equilibrium Compositions, Rocket Performance, Incident and Reflected Shocks, and Chapman-Jouguet Detonations; NASA-SP-273; NASA Lewis Research Center, 1976.

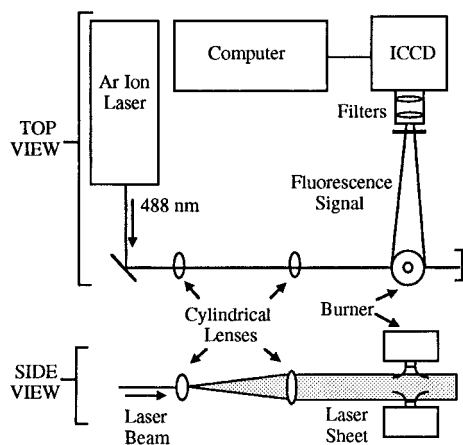


**Figure 5.** Schematic diagram of PLIF system. The top view shows the entire PLIF setup, while the side view shows the laser sheet expansion.

energy transfer occurred in the excited electronic state, resulting in fluorescence from a broad range of upper vibrational and rotational levels. Since the buffer gas pressure is much higher in our studies, extensive vibrational and rotational energy transfer is expected. With the spectroscopic constants of  $\text{KH}^{25}$  and the equations for diatomic energy levels of Huber and Herzberg,<sup>31</sup> we calculate the wavelength range within which KH observed  $\text{Na}_2$  fluorescence to be from 460 to 566 nm, in agreement with our observations. Structure is visible in the fluorescence and, although the spectrum is severely overlapped, the most intense peaks appear at intervals of roughly 4 nm, which is roughly the spacing between a series of vibrational bands emitted by a common upper vibrational level in the  $\text{Na}_2$  molecule. These results led to the conclusion that the LIF signal is indeed from  $\text{Na}_2$ .

Interestingly, an enhanced Na signal at 589 nm was observed through the monochromator when 488 or 514.5 nm argon ion laser light or 632.8 nm HeNe light was directed through the reaction zone, indicating that photodissociation was occurring. 488 nm light populates the  $B^1\Pi_u$  state, which is crossed by the weakly bound  $C^1\Pi_g$  state.<sup>30</sup> If electronic energy transfer occurred from the B state to the upper vibrational levels of the C state, the  $\text{Na}_2$  could dissociate to form excited Na, which would subsequently emit. The 632.8 nm HeNe beam excites the  $\text{Na}_2$  into the  $A^1\Sigma_u^+$  state,<sup>32</sup> but it is not clear by what mechanism this would eventually lead to 589 nm emission.

**PLIF Spectroscopic Studies.** Planar LIF (PLIF) involves forming the laser beam into a two-dimensional sheet before passing it through the region of interest. A camera is used to collect the emitted light to give a two-dimensional image of the reactive species' spatial distribution and relative concentration. In the experimental arrangement shown in Figure 5, the 488.0 nm continuous light from a 5 GHz bandwidth argon ion laser was formed into a collimated vertical sheet with a 25 mm focal length cylindrical expanding lens and a 500 mm focal length cylindrical focusing lens. The sheet was clipped to 9.1 mm high and 1.5 mm wide by passing it through circular apertures and vertical slits, before directing it through the center of the reaction zone. The fluorescence was collected perpendicular to the illumination plane and focused onto an intensified, cooled CCD (ICCD) camera ( $576 \times 384$  pixels, each  $23 \mu\text{m}$  square) using an  $f/4.5$  lens. ICCD images generally consist of an average of between 50 and 150 exposures, each of which was temporally integrated over a  $100 \mu\text{s}$  intensifier gate interval. Images were spatially averaged  $2 \times 2$  pixels to give a nominal axial and radial resolution of 0.01 cm. For the  $\text{Na}_2$  PLIF measurements, atomic Na emission at 589 nm was

**Table 1. Strain Rates and Reactant Mole Fractions**

reactants	strain rate ( $\text{s}^{-1}$ )	chloride mol % in Ar	sodium mol % in Ar <sup>a</sup>
Na/TiCl <sub>4</sub> /Ar	316 (high)	0.1, 0.005, 0.0	0.1
Na/TiCl <sub>4</sub> /Ar	85 (low)	0.07, 0.01, 0.0	0.1
Na/BCl <sub>3</sub> /Ar	316 (high)	0.2, 0.1, 0.05, 0.005, 0.0	0.1
Na/BCl <sub>3</sub> /Ar	85 (low)	0.15, 0.04, 0.01, 0.0	0.1

<sup>a</sup> This Na mole percent is only an upper limit. The value for Na mole percent used in modeling is 0.02%.

filtered out using a short-pass 550 nm interference filter with a rejection ratio of 1000:1, and the 488 nm laser light was rejected with a Schott glass long-pass filter. Thus, light between wavelengths of 500 and 550 nm was collected. Under each set of flow and concentration conditions, images were also taken with the long-pass filter removed, which allowed the 488 nm scattered light to be imaged. This allowed monitoring of light scattering resulting from particle formation. Additional images were taken using 514.5 nm argon ion laser light to excite  $\text{Na}_2$ . In these, both  $\text{Na}_2$  fluorescence and scattered light were collected and imaged using a 514.5 nm, 10 nm bandwidth interference filter. These images were in good agreement with the 488 nm data but turned out to be much more noisy and are not shown. Spatial uniformity of the 0.14 W laser beam used in all experiments was monitored during the experiments by using a beam splitter to direct a 5% reflection of the laser sheet through a static dye cuvette containing rhodamine 6G laser dye in methanol. The resulting fluorescence image was recorded using a video CCD camera with a framegrabber computer board. To analyze the ICCD images, a background image of flame emission was first taken with the laser blocked and was subtracted from the raw fluorescence image. Next, the image was normalized to the detector spectral response and flat-field uniformity, based on prior measurements.<sup>21</sup> The image was then corrected for the laser energy distribution by remapping images of the static dye cuvette from the video CCD to the ICCD coordinates. Excited-state electronic quenching was assumed to be constant, since under our experimental conditions the temperature was constant, and the gas flows were greater than 99.7% Ar.

PLIF measurements of  $\text{Na}_2$  were taken under varying flow conditions and reactant concentrations, as presented in Table 1. Global strain rate, which is inversely proportional to the time available for reaction, was calculated as the mean exit velocity divided by half the separation distance between the two innermost tubes of the reactor. Flows with higher strain rates have lower times available for reaction.

The Ar flow over the molten Na was sufficiently fast that it could not be assumed to be saturated with Na. To determine the upper limit on the Na concentration, the Ar flow rate was decreased while monitoring the  $\text{Na}_2$  PLIF signal. As Ar flow rate was decreased, the  $\text{Na}_2$  signal increased, indicating a higher concentration of  $\text{Na}_2$  vapor in the Ar. At the point where the  $\text{Na}_2$  fluorescence signal became independent of Ar flow rate, it was assumed that the Ar was saturated with Na/ $\text{Na}_2$ . The concentration of  $\text{Na}_2$  and the Na/ $\text{Na}_2$  equilibrium composition at saturation are known,<sup>33</sup> and, under our conditions, the  $\text{Na}_2$  PLIF signal intensity should be linear with  $\text{Na}_2$  concentration. Assuming saturation, these conditions allow us to make an absolute calibration of the  $\text{Na}_2$  concentration and to define an upper limit for Na concentration. The determination of the saturation point, however, was complicated by the fact that the flow field became unstable at very low flow rates.

Additional experiments were performed to visualize the flow field by seeding the chloride flow with  $\text{Al}_2\text{O}_3$  particles and imaging the 488 nm laser light scattered off these particles. A photograph of the flame during these experiments is shown in Figure 6, where it is seen that the flow field is symmetric, steady, and well-defined. Samples of the particles produced

(31) Huber, K. P.; Herzberg, G. *Molecular Spectra and Molecular Structure IV. Constants of Diatomic Molecules*; Van Nostrand Reinhold: New York, 1979; Vol. 4.

(32) Johnson, S. E.; Sakurai, K.; Broida, H. P. *J. Chem. Phys.* **1970**, *52*, 6441.

(33) Chase, M. W., Jr.; Davies, C. A.; Downey, J. R., Jr.; Frurip, D. J.; McDonald, R. A.; Syverud, A. N. *JANAF Thermochemical Tables*, 3rd ed.; American Chemical Society and the American Institute of Physics for the National Bureau of Standards: Midland, MI, 1986.

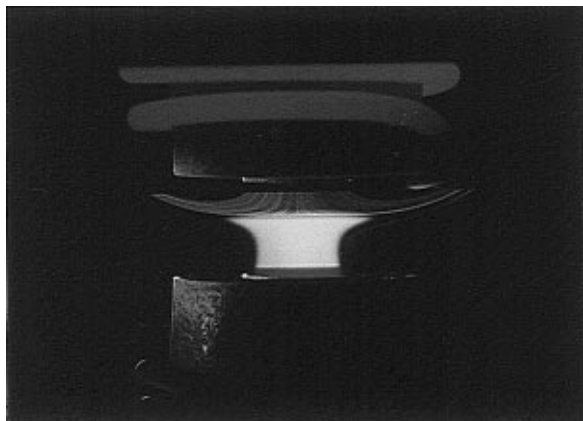


**Figure 6.** Photograph of flame during visualization of the flowfield. The upper flow is seeded with  $\text{Al}_2\text{O}_3$  particles and illuminated with 488 nm laser light.

**Table 2. Reaction Mechanism and Rate Constants**

reaction	A factor ( $\text{cm}^3 \text{mol}^{-1} \text{s}^{-1}$ )	activation energy (kJ/mol)
$\text{BCl}_3 + \text{Na} \rightarrow \text{BCl}_2 + \text{NaCl}$	$1 \times 10^{14}$	33.1
$\text{BCl}_2 + \text{Na} \rightarrow \text{BCl} + \text{NaCl}$	$1 \times 10^{14}$	0
$\text{BCl} + \text{Na} \rightarrow \text{B} + \text{NaCl}$	$1 \times 10^{14}$	131.4
$\text{B} + \text{B} \rightarrow 2\text{B}_{(s)}$	$1 \times 10^{12}$	0
$\text{TiCl}_4 + \text{Na} \rightarrow \text{TiCl}_3 + \text{NaCl}$	$1 \times 10^{14}$	0
$\text{TiCl}_3 + \text{Na} \rightarrow \text{TiCl}_2 + \text{NaCl}$	$1 \times 10^{14}$	14.7
$\text{TiCl}_2 + \text{Na} \rightarrow \text{TiCl} + \text{NaCl}$	$1 \times 10^{14}$	103.4
$\text{TiCl} + \text{Na} \rightarrow \text{Ti} + \text{NaCl}$	$1 \times 10^{14}$	31.4
$\text{Ti} + \text{Ti} \rightarrow 2\text{Ti}_{(s)}$	$1 \times 10^{12}$	0
$\text{Na} + \text{Na} \leftrightarrow \text{Na}_2$	$1.5 \times 10^{12}$	0
$\text{NaCl} + \text{NaCl} \rightarrow 2\text{NaCl}_{(s)}$	$1 \times 10^{13}$	0

in the  $\text{TiCl}_4$  flames were obtained for characterization with transmission electron microscopy (TEM), energy-dispersive X-ray spectroscopy (EDS), and X-ray diffraction (XRD). Samples were not extracted from the  $\text{BCl}_3$  flames, because our EDS instrument is not equipped with a window which passes the wavelengths necessary for B detection.

**Modeling.** In addition to the experimental simplifications afforded by the use of the counterflow reactor, modeling is significantly simplified because the flow field can be reduced to a one-dimensional problem. This implies that a model incorporating detailed kinetics and transport is considerably more tractable. Indeed, several computer models exist which model this particular geometry. Our calculations were performed using the Sandia counterflow diffusion flame code,<sup>22</sup> which solves the boundary layer equations for mass, energy, momentum, and chemical species, along the stagnation streamline. Inputs to the model include the boundary velocities and temperatures and separation distance. The user also specifies the relevant species, their thermochemistry, transport properties (diffusivity, thermal conductivity, and viscosity), and chemical kinetic data. As constructed, the model does not include provisions for particle nucleation and growth. The output of the code is species concentration as a function of axial location in the reactor, suitable for comparison with experimental measurement.

The conditions specified in the simulations are shown in Table 1. The notable exception is that the Na mole fraction used in the final simulations was 0.02%, as explained in the Discussion. Diffusion coefficients were estimated for the chlorinated metal species by taking the diffusion coefficients of the corresponding chlorinated carbon species<sup>34</sup> and mass scaling them by the metal halide atomic weight. The proposed reaction mechanism is shown in Table 2 and involves a simple sequential abstraction of chlorine by sodium. The rate constants for the first abstraction reactions for  $\text{TiCl}_4$  and  $\text{BCl}_3$

have been determined experimentally.<sup>16</sup> In both cases the A factors (preexponential factors) for the initiation reactions were found to be consistent with simple abstraction reactions ( $10^{14} \text{ cm}^3 \text{ mol}^{-1} \text{ s}^{-1}$ ). For  $\text{TiCl}_4$ , the measured rate was  $9.9 \times 10^{13} \text{ cm}^3 \text{ mol}^{-1} \text{ s}^{-1}$  at 543 K. Such a large rate constant at moderate temperatures implies that the activation energy must be small, and since this initiation reaction is exothermic, we can reasonably assume an activation barrier of near zero. For the boron reaction, the rate constant measured was considerably smaller ( $4.7 \times 10^{11} \text{ cm}^3 \text{ mol}^{-1} \text{ s}^{-1}$ ) than the corresponding titanium reaction; however, the abstraction reaction leading to  $\text{BCl}_2$  is endothermic by about 33 kJ/mol. Assuming this as the activation energy, we calculate an A factor of  $6.7 \times 10^{14} \text{ cm}^3 \text{ mol}^{-1} \text{ s}^{-1}$ . This result is consistent with the titanium reaction since we expect that the transition states for both reactions should be similar and, therefore, they should have similar A factors. The differences are well within experimental error, since at 550 K an error of only 8.4 kJ/mol (2 kcal/mol) in the activation energy translates into an error in the rate constant of a factor of 6. Thus, we assume that the A factors for this type of reaction should be around  $10^{14}$  and that subsequent abstractions will have similar A factors. We further assume that all elementary steps proceed with activation energies equal to the endothermicity of the reaction as determined by the JANAF tables.<sup>33</sup> Furthermore, since there is a fast sink term (namely particle nucleation), these reactions can be considered irreversible. The rates for condensation of B, Ti and NaCl into  $\text{B}_{(s)}$ ,  $\text{Ti}_{(s)}$ , and  $\text{NaCl}_{(s)}$ , respectively, are estimated to occur with no activation barrier and A factors of ( $1 \times 10^{12}$ – $1 \times 10^{13}$ )  $\text{cm}^3 \text{ mol}^{-1} \text{ s}^{-1}$ . These reactions were included only to serve as markers to identify where in the reactor particle nucleation would be initiated. The only reversible reaction in the mechanism is the dimerization of sodium ( $2\text{Na} \leftrightarrow \text{Na}_2$ ), which serves to produce  $\text{Na}_2$  when Na is being consumed and provides the marker species to compare with experiment. The rate of sodium dimerization was found to have a negligible effect on the results and is estimated to be  $1.5 \times 10^{12} \text{ cm}^3 \text{ mol}^{-1} \text{ s}^{-1}$ .

## Results

Figure 7a,b shows ICCD images of the flow region with no chloride and with  $\text{BCl}_3$  added to the upper stream, respectively. The images include both  $\text{Na}_2$  PLIF and also 488 nm elastically scattered laser light. In each image, the thick central signal is due to  $\text{Na}_2$  PLIF, as indicated in Figure 7a. In addition, two “wings” are visible on either side of the  $\text{Na}_2$  PLIF. Because the shroud gases are cooler than the inner reactive gas streams, Na condenses where the hot Na vapor stream contacts the cooler Ar shroud. The visible “wings” are most likely caused by laser light scattered from the condensing sodium. As shown in Figure 7b, the addition of  $\text{BCl}_3$  causes the appearance of a thin horizontal band of light, visible near the stagnation plane, resulting from laser light scattered from particles being formed by the reaction of Na and  $\text{BCl}_3$ . Images of Na reacting with  $\text{TiCl}_4$  are qualitatively the same and are not shown.

To examine the effect of changing the flow rate and chloride initial concentrations, axial profiles of  $\text{Na}_2$  PLIF and scattered light along the vertical centerline (stagnation streamline) of the reactor were examined. Figures 8–11 show profiles of  $\text{Na}_2$  PLIF, including 488 nm scattered light, versus the distance between the reactor flow tubes with a resolution of  $\pm 0.01$  cm for high and low strain rates, and the chloride mole fractions given in Table 1. The experimental profiles are shown with solid lines and labeled with their respective chloride mole fractions. Figures 8 and 9 depict the  $\text{TiCl}_4$  data, and Figures 10 and 11 depict the  $\text{BCl}_3$  data at low and high strains, respectively. It is evident that both the

(34) Kee, R. J.; Dixon-Lewis, G.; Warnatz, J.; Coltrin, M. E.; Miller, J. A. A Fortran Computer Code Package for the Evaluation of Gas-Phase Multicomponent Transport Properties. *Sandia Rept. SAND86-8246*; Sandia National Laboratories, 1988.

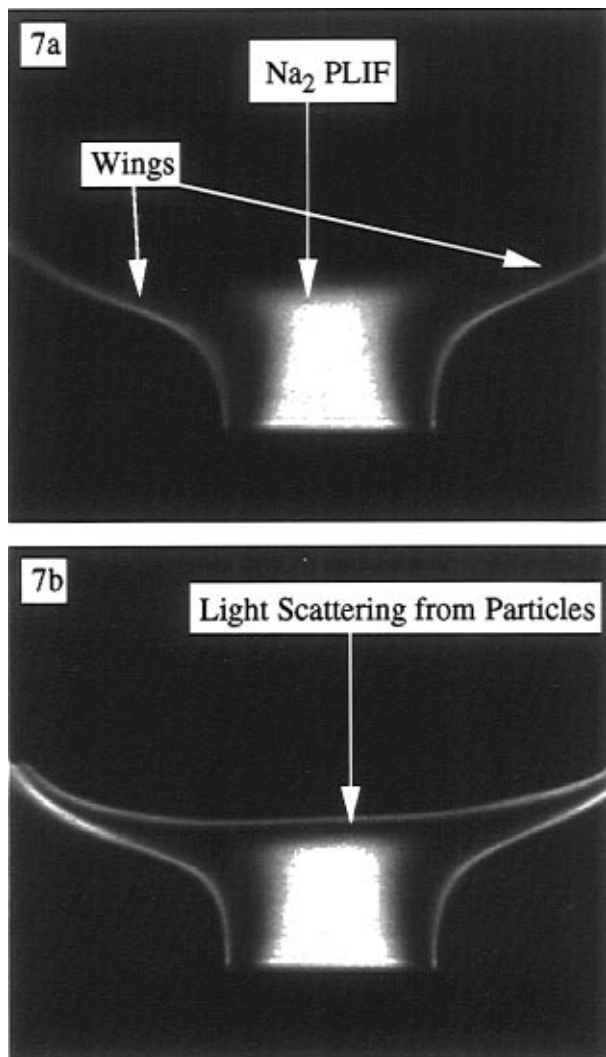


**Figure 7.** ICCD image of  $\text{Na}_2$  PLIF and 488 nm scattered light with (a) no chloride added to the upper Ar stream and (b) with  $\text{TiCl}_4$  added to the upper Ar stream, resulting in particle formation and light scattering.

slope and position of the  $\text{Na}_2$  profile depend on reactant concentration and strain rate. In both the  $\text{TiCl}_4$  and  $\text{BCl}_3$  low strain rate cases, light scattering from particles indicates the position of the stagnation plane. In Figures 8 and 10, the location of the stagnation plane is denoted as a range, since its position is known only within the experimental resolution.

The corresponding model simulation results are shown with dotted lines in Figures 8–11 and will be examined in the Discussion. To compare the model results to the experimental profiles, a correction to the model vertical axis was applied to match the position of the model stagnation plane to that of the experiment, since model boundary conditions may not accurately represent the true conditions, as addressed in the Discussion. In Figures 8–11, the experimental vertical axis has been shifted by between 0.10 and 0.25 cm, so that the  $\text{Na}_2$  model and experimental profiles with no chloride added are coincident.

As shown in Figure 1, the reaction of Na with  $\text{TiCl}_4$  can produce nanoscale Ti particles encased in NaCl. Although the coflow reactor is of a geometry different from the counterflow reactor employed in the present experiments, the chemical processes occurring are similar. Particles were thermophoretically sampled (via

rapid insertion of a TEM grid) in the counterflow reactor during the present experiments, and subsequent TEM/EDS analysis indicated that cubic particles, ranging in size between 15 and 60 nm, as shown in Figure 12, were formed which included Ti, Na, Cl, and O. One possible cause of the presence of O in the samples was the method of sample extraction, which may have caused entrainment of air or subsequent oxygen contamination. Particles were also collected for XRD analysis by inserting a quartz slide into the reactive zone of the counterflow reactor. The XRD results show crystalline NaCl with some broad unidentified background peaks, which are most likely due to the quartz slide. Because the counterflow flame is typically about 450 K cooler than the coflow flame, one expects that smaller Ti particles with smaller grain size are produced in the counterflow reactor. Indeed, XRD did not show any distinctive Ti structure. Although well suited for investigation of the physical/chemical processes in the sodium/halide flames, this reactor geometry is limited in its ability to produce significant quantities of materials.

### Discussion

As shown in Figures 8–11, increasing metal chloride concentration results in a displacement of the  $\text{Na}_2$  profile toward the Na input tube, and the slope of the  $\text{Na}_2$  profile becomes steeper. The profiles become displaced and change slope so that the transport rate of material matches the consumption rate of metal chloride and Na by reaction. The profile displacement with increasing metal chloride concentration results from the increase in diffusive flux of the metal chloride, which drives the reaction zone toward the sodium, thus increasing the concentration gradient and flux of the sodium. The high strain profiles for both  $\text{TiCl}_4$  and  $\text{BCl}_3$  precursors in Figures 9 and 11, respectively, show smaller changes in slope and displacement with increasing metal chloride concentration than the corresponding low strain profiles in Figures 8 and 10.

The dominant factors affecting the slope and position of the profiles can be identified by comparing the experimental profiles to those obtained through modeling. Initial modeling efforts gave profiles which were of similar slope to experimental profiles; however, the relative displacement of the modeled profiles disagreed with that of the experimental profiles. For the profile with the highest chloride loading, the displacement in the model was up to 0.04 cm less than in the experiment, relative to the profile with no chloride. The model and experimental profiles with higher chloride loadings showed similar displacements, relative to the profile with the lowest chloride loading. Input parameters to the model were then scrutinized to determine possible sources for this discrepancy. One parameter not well-known is the Na dimerization rate. To test the sensitivity of the model to the Na dimerization rate, we decreased the rate by a factor of 1500 and found only a minimal effect. The metal chloride concentration has a strong influence on the profiles; however, the concentrations are sufficiently well-known to preclude this as a possible source for the discrepancies. One input in doubt is the concentration of Na. As previously discussed, the value quoted in Table 1 for the Na mole fraction is an upper limit. Decreasing the Na concentration in the model results in greater displacement

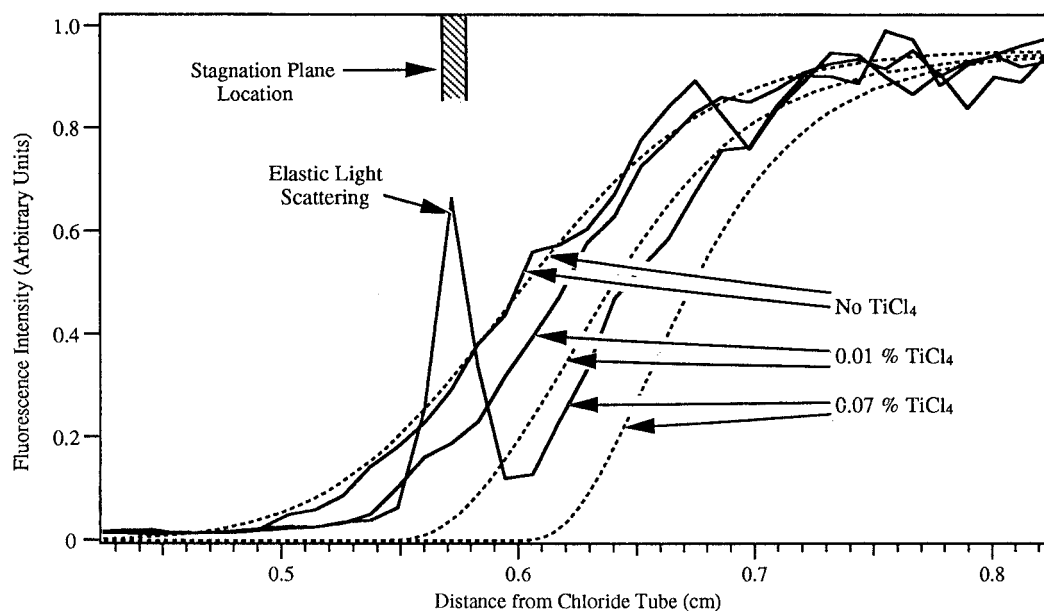


**Figure 8.** Profiles of  $\text{Na}_2$  PLIF and 488 nm scattered light along the vertical centerline for low strain rate  $\text{TiCl}_4/\text{Na}$  mole fractions in Table 1. Model profiles are shown with dotted lines and data is shown with solid lines. The  $x$  axis is the experimental distance from the chloride (or upper) flow tube with a resolution of  $\pm 0.01$  cm. Peaks are due to 488 nm scattered light.

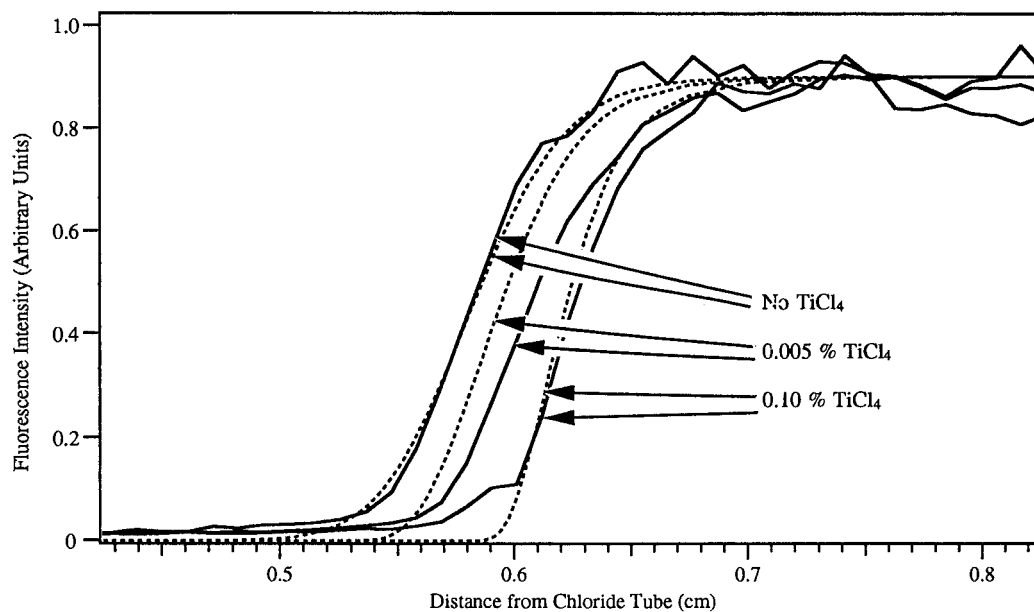


**Figure 9.** Profiles of  $\text{Na}_2$  PLIF and 488 nm scattered light along the vertical centerline for high strain rate  $\text{TiCl}_4/\text{Na}$  mole fractions in Table 1. Model is dotted lines, and data are solid lines, and the  $x$  axis has a resolution of  $\pm 0.01$  cm.

relative to the profile with no chloride but causes little change in the displacement between profiles with differing amounts of chloride. By comparing the experimental and model profiles, it appeared that the assumed Na concentration was too high by about a factor of 5. This is consistent with incomplete saturation of the Ar carrier gas with Na vapor. The model profiles shown in Figures 8–11 were calculated with a Na mole fraction of 0.02%, instead of 0.1%. Once this change was made, good agreement was obtained between the model and experiment, considering the  $\pm 0.01$  cm resolution of the experimental profiles.

In this reactor configuration, the product formation rate can be limited by the rate of transport (diffusion and convection) or by the rate of the intrinsic chemistry. The Na/chloride reaction rates were varied to determine whether chemical reaction rate or transport properties

had a greater effect on the processes occurring in the reactor. To find an upper limit for displacement at very fast reaction rates, the activation energies ( $E_a$ ) were decreased for the reactions of Na with  $\text{TiCl}_x$  at low and high strain rates (for the highest  $\text{TiCl}_4$  concentrations). Setting  $E_a(\text{Na} + \text{TiCl}_2)$  to zero produced profiles which were displaced to the right by 0.015 and 0.010 cm for low and high strain rates, respectively, relative to the profiles with  $E_a(\text{Na} + \text{TiCl}_2) = 103.4$  kJ/mol. For both high and low strain rate cases, there was no difference between setting all  $E_a(\text{Na} + \text{TiCl}_x)$  to zero and setting only  $E_a(\text{Na} + \text{TiCl}_2)$  to zero. Thus, the  $\text{Na} + \text{TiCl}_2$  reaction can be considered the rate-limiting step. When the rate for  $\text{Na} + \text{TiCl}_2$  was increased by a factor of 10 in addition to having set  $E_a(\text{Na} + \text{TiCl}_2)$  to zero, there was no additional displacement of the profile, implying that at this high rate, the chemistry is diffusion limited.

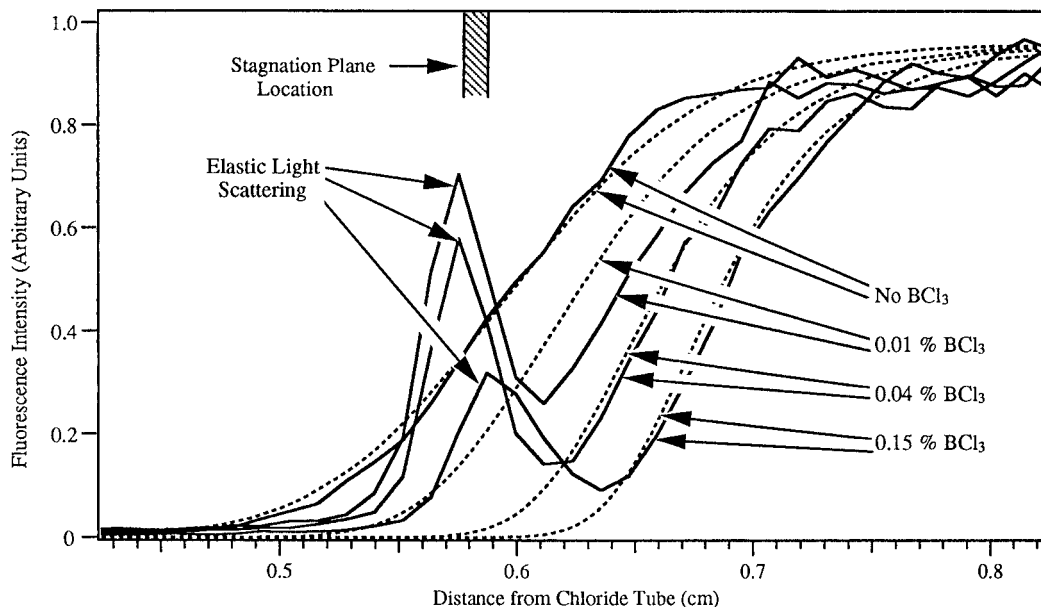


**Figure 10.** Profiles of  $\text{Na}_2$  PLIF and 488 nm scattered light along the vertical centerline for low strain rate  $\text{BCl}_3/\text{Na}$  mole fractions in Table 1. Model is dotted lines, and data are solid lines, and the  $x$  axis has a resolution of  $\pm 0.01$  cm. Peaks are due to 488 nm scattered light.

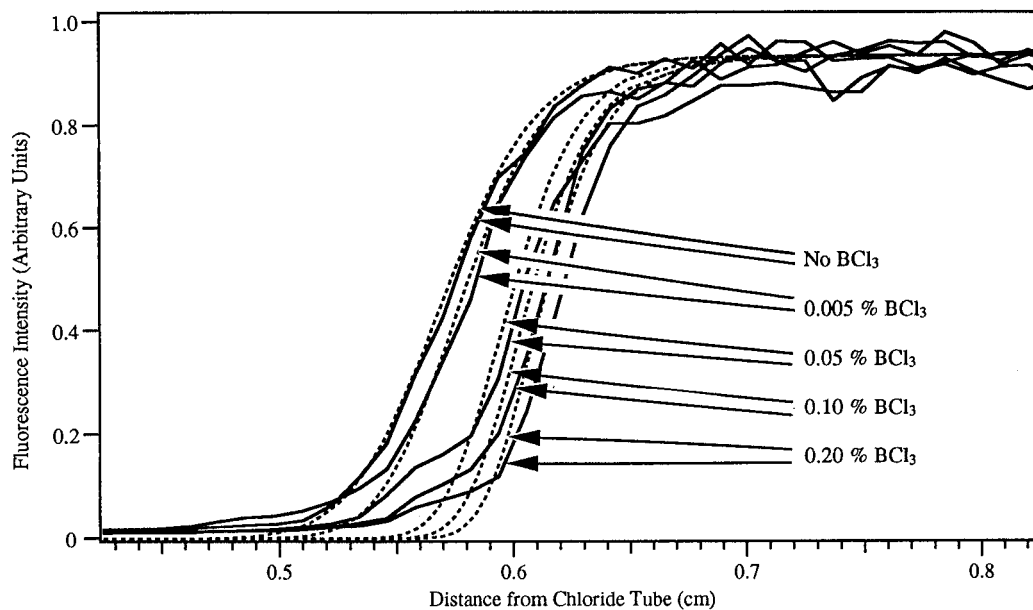


**Figure 11.** Profiles of  $\text{Na}_2$  PLIF and 488 nm scattered light along the vertical centerline for high strain rate  $\text{BCl}_3/\text{Na}$  mole fractions in Table 1. Model is dotted lines, and data are solid lines, and the  $x$  axis has a resolution of  $\pm 0.01$  cm.

When the  $\text{Na} + \text{TiCl}_2$  reaction rate was decreased a factor of  $10^{10}$  with  $E_a(\text{Na} + \text{TiCl}_2) = 103.4$  kJ/mol, the resulting profiles were identical with those with no chloride, implying that at these slow rates, the characteristic reaction time was much larger than the time for convection. The model profiles displayed in Figures 8 through 11 are closer to the diffusion-limited case, indicating that the chemistry occurring in the system is quite fast. The slopes of the model  $\text{Na}_2$  profiles with no chloride agree very well with the slopes of the experimental profiles, indicating that the diffusion rates computed for  $\text{Na}$  and  $\text{Na}_2$  are accurate. In general, the model profiles are not as sensitive to reaction rates as they are to the input concentration of the reactants.

Light scattering from particles is evident in the profiles, particularly at low strain rates. Scattering intensity,  $I(t)$ , is proportional to the product of number density and particle diameter to the sixth power. In

the limit of coagulation/coalescence dominated growth, the temporal dependence can be expressed<sup>35</sup> as follows:

$$I(t) \propto Nd^6 = N_0 d_0^6 (1 + N_0 K t) \quad (2)$$

where  $N$  is particle number density,  $d$  is diameter,  $K$  is the coagulation coefficient,<sup>35</sup>  $t$  is time, and the subscript 0 refers to conditions at  $t = 0$ . Thus, scattering intensity increases with time due to coagulation/coalescence effects. A low scattering intensity can result from either a small extent of initial reaction (total mass of particulate material formed) or alternatively from a short time for coagulation processes. These points are illustrated in the low and high strain rate profiles with  $\text{TiCl}_4$  in

(35) Hinds, W. C. *Aerosol Technology: Properties, Behavior, and Measurement of Airborne Particles*; John Wiley and Sons, Inc.: New York, 1982.

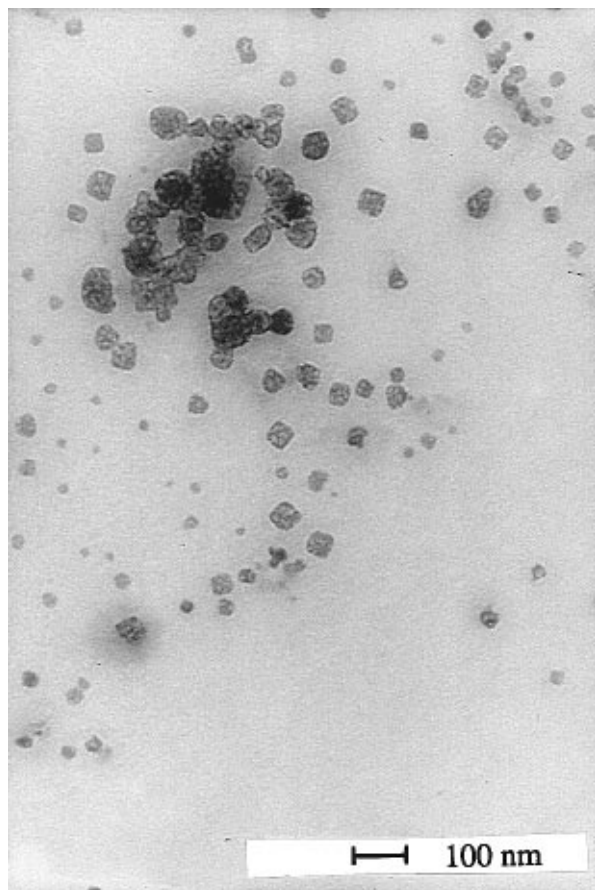


**Figure 12.** TEM image of cubic NaCl particles collected in the counterflow reactor.

Figures 8 and 9. For the low strain conditions in Figure 8, a negligible amount of elastic scattering is observed for 0.01%  $\text{TiCl}_4$ , but with 0.07%  $\text{TiCl}_4$ , particle formation is evident at 0.57 cm. The increase in chloride concentration increases product formation rates and, thus, scattering intensity. Comparing the high and low strain rate conditions, the effects of residence time for coagulation can be seen. Residence time varies inversely with strain rate so the low strain rate reacting flows in Figure 8 have greater time for coagulation than those with high strain rate in Figure 9. Consequently, the scattering signal for the low strain rate flow with 0.07%  $\text{TiCl}_4$  is greater than that for the high strain rate flow with 0.10%  $\text{TiCl}_4$ .

In Figure 10 the scattering intensity is seen to actually decrease with increasing  $\text{BCl}_3$  concentration. The particle formation rate increases with increasing  $\text{BCl}_3$  concentration, so the decrease in light scattering from particles is apparently due to a decrease in the time available for coagulation. One explanation for this is that the particles are produced on the  $\text{BCl}_3$  side of the stagnation plane, such that increasing the  $\text{BCl}_3$  concentration moves the particle production zone closer to the stagnation plane, possibly crossing it, with a corresponding lower residence time for coagulation and lower light scattering intensity. This hypothesis is consistent with an increase in  $\text{BCl}_3$  concentration leading to smaller particles yet higher conversion rates. In the case of  $\text{TiCl}_4$  in Figure 8, the light scattering increases with increasing  $\text{TiCl}_4$  concentration. This is consistent with the particle production occurring on the Na side of the stagnation plane such that as  $\text{TiCl}_4$  concentration is increased, the particle production rate

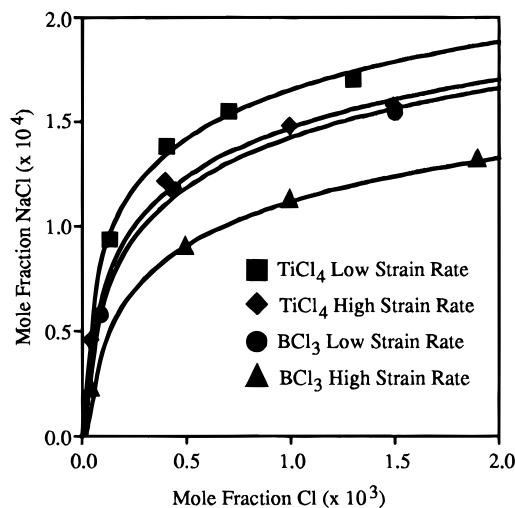


**Figure 13.** Maximum mole fraction of NaCl versus mole fraction of Cl supplied for high and low strain rate conditions with  $\text{BCl}_3$  and  $\text{TiCl}_4$ .

increases and the production zone moves further from the stagnation plane, allowing additional time for coagulation to occur and resulting in greater scattering intensity.

In the modeling results, the relative positions of peak NaCl formation and stagnation plane can be examined. The model shows that for a  $\text{TiCl}_4$  concentration of 0.01%, peak NaCl formation occurs very close to the stagnation plane giving little time for coagulation, while for  $\text{TiCl}_4 = 0.07\%$ , the peak NaCl formation occurs further from the stagnation plane on the Na side, allowing more time for coagulation. This is consistent with the result that more light scattering is visible in the higher  $\text{TiCl}_4$  concentration case because of longer time available for coagulation and higher initial particle production rates. For  $\text{BCl}_3$ , the modeling results indicate that for 0.01%  $\text{BCl}_3$  concentration, peak NaCl formation occurs on the  $\text{BCl}_3$  side. For intermediate  $\text{BCl}_3$  concentration (0.04%), peak NaCl formation occurs on the Na side, and for the highest  $\text{BCl}_3$  concentration (0.15%), peak NaCl formation occurs on the Na side, further from the stagnation plane. Thus, the model results show the proper trend (i.e., particle formation for low  $\text{BCl}_3$  concentration occurring on the  $\text{BCl}_3$  side and moving toward the Na side with increasing  $\text{BCl}_3$  concentration), although the position of particle formation is too close to the Na side relative to the stagnation plane to account for the elastic scattering intensities. This discrepancy presumably results from improper boundary conditions used in the model, which assumes that the flows exiting the nozzles are plug flow, whereas the real flow conditions are most likely somewhere between plug and fully developed flow. In addition, the Na concentrations are not precisely known, as was previously noted, and the model has no provision to account for buoyancy effects and assumes true isothermal conditions. Despite the shift in the position of particle formation relative to the stagnation plane, the model obviously captures the essence of the features seen in the experiment.

The model can also be used to extract information on the mechanism by which formation of  $\text{TiB}_2$  particles is likely to occur. Figure 13 displays the maximum mole fraction of NaCl produced versus the mole fraction of chloride input for several different chloride concentra-

tions. Results are shown for high and low strain rates for both  $\text{TiCl}_4$  and  $\text{BCl}_3$  precursors. In all cases, the mole fraction of NaCl produced levels off at high mole fraction of chloride, as Na becomes the limiting reagent. As shown in Figure 13, the conversion efficiency was greater for the low strain case than for the high strain case, in keeping with the longer time available for reaction. The titanium precursor appears to have reacted faster than the boron precursor, although the differences are small. In addition, the model indicates that the axial location of metal production is similar for both precursors under similar conditions, implying that particle formation of  $\text{TiB}_2$  may begin from gas-phase clustering reactions rather than nucleation of one component followed by gas-cluster reactions between the two components. The relative equivalence of rates should be expected for a wide variety of precursors due to the high reactivity of Na with metal chlorides. As such, one should expect that multicomponent particles may be made without the need for post processing after NaCl removal because of the chemically homogeneous nature of the growth process outlined.

### Conclusions

PLIF proved to be a sensitive, nonintrusive method of examining changes in the concentration of  $\text{Na}_2$ , which

were related to the Na chemistry through chemical equilibrium. The spatial distribution of  $\text{Na}_2$  and the light scattered from particles was found to be sensitive to both flow rate and metal chloride concentration which influence the particle production rates of the reacting flows. Modeling was used to provide insight into the processes occurring in the reacting flow; good agreement was obtained between model and experiment using a stepwise chlorine abstraction model. Modeling results revealed that the chemical reaction rates in this system are very fast. The model's implication for the formation of  $\text{TiB}_2$  is that gas-phase clustering reactions involving both components is the most likely mechanism. Future studies include observing the reacting flow under reduced pressure conditions which would better resolve the profiles and retard the reaction rates to better study the chemistry of the system.

**Acknowledgment.** The authors wish to acknowledge the valuable help of Dr. B. K. McMillin regarding the optical detection and data analysis via the ICCD camera and Ms. M. I. Aquino regarding TEM and XRD sample collection. Partial support for D.P.D. was provided by the NSF.

CM9600844